A pressure core based characterization of hydrate-bearing sediments in the Ulleung Basin, Sea of Japan (East Sea)

Tae Sup Yun,[1] Changho Lee,[2] Jong-Sub Lee,[3] Jang Jun Bahk,[4] and J. Carlos Santamarina[2]

Received 15 February 2010; revised 22 November 2010; accepted 9 December 2010; published 15 February 2011.

[1] The physical characteristics of hydrate-bearing sediments sampled by pressure coring from the Ulleung Basin in the Sea of Japan (East Sea) were investigated using an instrumented chamber capable of testing recovered natural sediments that have never left the methane hydrate stability field. The heterogeneous distribution of segregated hydrate veins and lens structures in sediments results in highly variable geophysical and geomechanical properties. The scaled production test was conducted by controlled depressurization of pressure cores while dissociation and gas production were concurrently monitored using various sensors in the instrumented chamber. The hydrate saturation was estimated to be ~19.5% in the pore space. Data show a sharp reduction in sediment shear and bulk stiffnesses during hydrate dissociation. Relatively fast gas migration was observed, probably along high-conduction planes left behind as hydrate veins dissociated. The spatial distribution of hydrates in sediment was analyzed based on 3-D image processing. The phenomena relevant to the production test and sampling effects during pressure coring are discussed.

Citation: Yun, T. S., C. Lee, J.-S. Lee, J. J. Bahk, and J. C. Santamarina (2011), A pressure core based characterization of hydrate-bearing sediments in the Ulleung Basin, Sea of Japan (East Sea), *J. Geophys. Res.*, *116*, B02204, doi:10.1029/2010JB007468.

1. Introduction

[2] National efforts to identify alternative energy resources in South Korea have led to the exploration and investigation of gas hydrate-bearing sediments in the Ulleung Basin, Sea of Japan (East Sea), where gas charged sediments and pockmarks hint at the abundance of gas hydrates [*Huh et al.*, 1999; *Kargl et al.*, 2006]. The analysis of seismic data reveals that gas hydrates in this region have formed by the upward migration of dissolved gas through fracture networks and chimneys beneath the stability field [*Haacke et al.*, 2009; *Stoian et al.*, 2008]. High hydrate concentrations, probably $S_h > 35\%$ of the pore volume, was estimated in Late Miocene sands near fractures, chimneys and cold vents [*Lee et al.*, 2005].

[3] Organic carbon and biogenic methane prevail in the deep sediments of the Ulleung basin [*Lee et al.*, 2008; *Ryu et al.*, 2009]. Sediments are mainly sandy soils in the shelf (massive sand and bioturbated sand) and clayey soils in the continental slope (laminated mud, slightly laminated mud, bioturbated mud, homogeneous mud with distinct tephra layers) [*Bahk et al.*, 2000; *Lee et al.*, 1993; *Park et al.*, 2003]. Dominant clay minerals in the Miocene shales and sandstones of the Ulleung Basin are illite and smectite, with some kaolinite and chlorite presumably resulting from hydrothermal events [*Hillier et al.*, 1996]. Available geotechnical properties for sediments in the lower slope of the Ulleung Basin (water depth >1400 m) are very limited. Classification data show MH (high plasticity silt) and OH sediments (organic clay of high plasticity) with more than 70% clay content and often ~10% organic matter [*Lee et al.*, 1993].

[4] The Korea UBGH01 Expedition during the summer and fall of 2007 was performed to assess the existence of gas hydrate-bearing sediments, to recover deep marine sediments containing gas hydrates, and to evaluate physical properties of hydrate-bearing sediments. To prevent hydrate dissociation during sampling and core handling, as required for the geophysical and geomechanical characterization of gas hydrate-bearing marine sediments, the Korea UBGH01 Expedition recovered pressure cores which were then tested using the Instrumented Pressure Testing Chamber (IPTC). This manuscript documents the geophysical and geomechanical characterization of pressure cores, production test by the controlled depressurization of pressure cores, and post-degassing sediment characterization.

2. Methods and Materials

[5] Hydrate-bearing sediments can be recovered without dissociating the hydrate phase by maintaining P-T conditions using "pressure coring" technology [*Pettigrew*, 1992].

[1]School of Civil and Environmental Engineering, Yonsei University, Seoul, South Korea.
[2]School of Civil and Environmental Engineering, Georgia Institute of Technology, Atlanta, Georgia, USA.
[3]Department of Civil, Environmental and Architectural Engineering, Korea University, Seoul, South Korea.
[4]Petroleum and Marine Resources Division, Korea Institute of Geoscience and Mineral Resources, Daejeon, South Korea.

0148-0227/11/2010JB007468

Seven pressure cores were recovered during the UBGH Expedition01 (four Fugro Pressure Cores-FPC and three HYACE Rotary Cores-HRC). These pressure cores were then transferred under in situ hydrostatic pressure into storage chambers and maintained at a hydrostatic fluid pressure of 15 MPa and temperature of 4°C. All seven cores were first characterized using 2-D X-ray images and 3-D X-ray CT images to evaluate the spatial distribution of gas hydrates within sediments.

[6] The physical characterization of pressure cores was conducted using Georgia Tech's Instrumented Pressure Testing Chamber (IPTC) [*Yun et al.*, 2006]. This device allows geophysical and geomechanical property measurements to be made in pressure cores without exposing the sediments to pressure or temperature conditions outside the methane hydrate stability field. Note that the effective stress the sediment experienced in situ is not maintained. The IPTC is instrumented to obtain P wave velocity ($f \approx 1$ MHz), S wave velocity ($f \approx$ 1–2 kHz), undrained shear strength (5.6 mm diameter penetrometer), electrical conductivity (2.1 mm diameter needle probe), and internal core temperature (1 mm diameter thermocouple) through perforations made through the plastic liner under in situ hydrostatic pressure. Figure 1 shows the complete test configuration, the IPTC chamber, and a close-up of the core inside the IPTC. The IPTC-based characterization took place within the core storage facility at the Korea Institute of Geoscience and Mineral Resources between 10 and 16 February 2008. The working temperature varied 3°C–5°C throughout the testing period.

[7] Six of seven recovered pressure cores were subjected to the IPTC-based characterization. Three cores were then selected for controlled depressurization within the IPTC. P and S wave velocities, electrical conductivity, temperature and the amount of produced gas were continuously measured during depressurization. A new set of longitudinal X-ray images were taken after depressurization to visually assess changes in sediment structure. Sediments from the depressurized cores were subjected to a comprehensive geotechnical study afterward [*Lee et al.*, 2011].

3. Results

[8] A summary of sediment characteristics is presented first, followed by the IPTC characterization and depressurization monitoring results.

3.1. Sediment Characterization: Index Properties

[9] We tested depressurized sediments to gather various fundamental properties including: specific gravity G_s, specific surface S_a, grain size distribution, liquid limit w_L, plastic limit w_P, X-ray diffraction, and scanning electron microscopy (SEM). Detailed test methods are given by *Lee et al.* [2011].

[10] Figure 2 presents two typical SEM (Hitachi S-4300) images. Samples were oven dried at 70°C and coated with a platinum layer. All images show a preponderance of microfossils, a wide range of diatom species, and framboidal pyrite. Diatoms are from 10 to 150 μm in size and most of them are partially broken, in part due to the high in situ vertical effective stress, estimated to be ~1 MPa. Intact diatoms rarely sustain 2 MPa [*Hong et al.*, 2006; *Tanaka and Locat*, 1999]. Clay minerals appear flocculated. Pyrite framboids are smaller than 20 μm, and their presence indicates a dysaerobic environment during sedimentation [*Kim et al.*, 2003].

[11] Index properties are summarized in Table 1. The dominant clay minerals were kaolinite and illite, and soils were classified as OH (organic clay of medium to high plasticity) or MH (diatomaceous silty clay) sediments with the mean grain size of $D_{50} \cong 3$ μm. Once again, the preponderant diatomaceous nature of these deposits is observed in SEM images.

3.2. Physical Characterization Inside the IPTC

[12] P wave and S wave velocities, electrical conductivity, and undrained shear strength were obtained for six pressure cores at selected locations along the core. Representative property profiles for the 10B-17P core are summarized in Figure 3. The following discussion applies to these data as well as similar results obtained for the other cores.

3.2.1. A 2-D X-Ray Image

[13] The bright bands indicate the presence of segregated hydrates, while the darker areas correspond to sediments (Figure 3a). There are irregularly spaced horizontal hydrate lenses with different thickness. Inclined veins are found at core positions of 30 and 40 cm, while vertical hydrate lenses are observed in the upper 0 to 40 cm of the core. Other cores show a similar vein and lens hydrate distribution.

3.2.2. P Wave Velocity

[14] The bulk stiffness of water governs the constrained modulus of water saturated soft sediments (Figure 3b). Thus, the P wave velocity V_P should be close to the propagation velocity in seawater V_P of ~1500 m/s, following Biot-Gassman asymptotic solution when the porosity of sediments is larger than ~0.4 (dashed line for reference is shown in Figure 3b). The solid circles denote the data collected at predefined locations, while the solid triangles are values specifically measured parallel to the hydrate veins. Higher velocities indicate the presence of high stiffness material such as hydrates. Most values measured along the core suggest a soft sediment, while V_P values measured parallel to horizontal hydrate veins at 30 cm and 40 cm locations (solid triangle) exhibit noticeably high wave velocities approaching ~3000 m/s (V_P of massive methane hydrate is 3750–3800 m/s [*Helgerud et al.*, 2009]). The solid line in Figure 3b shows onboard values measured in noncontact mode using lower frequency transducers placed outside the plastic liner (500 kHz, MultiSensor Core Logger operated by GeoTek Inc.). Unlike the IPTC measurements in direct contact with the sediment, the distinct horizontal hydrate veins located at 30 and 40 cm in the core are not detected by the noncontact measurements.

3.2.3. Shear Wave Velocity

[15] The shear wave velocity $V_s = \sqrt{G/\rho}$ (Figure 3c) reflects the sediment skeletal shear stiffness G and mass density ρ. The mean effective stress $\sigma'_m = (\sigma'_v + \sigma'_h)/2$ on the polarization plane, where σ'_v is vertical effective stress and σ'_h is horizontal effective stress, controls the skeletal shear stiffness in uncemented soils as $V_s = \alpha(\sigma'_m/kPa)^\beta$ [*Stokoe et al.*, 1992]. The selected reference value is estimated for an in situ vertical effective stress $\sigma'_v \approx 1.3$ MPa (the in situ depth of the core is ~136 m below seafloor (mbsf) and the corresponding mean effective stress σ'_m becomes ~1.04 MPa), and parameters $\alpha = 42$ m/s and $\beta = 0.3$ are adopted for

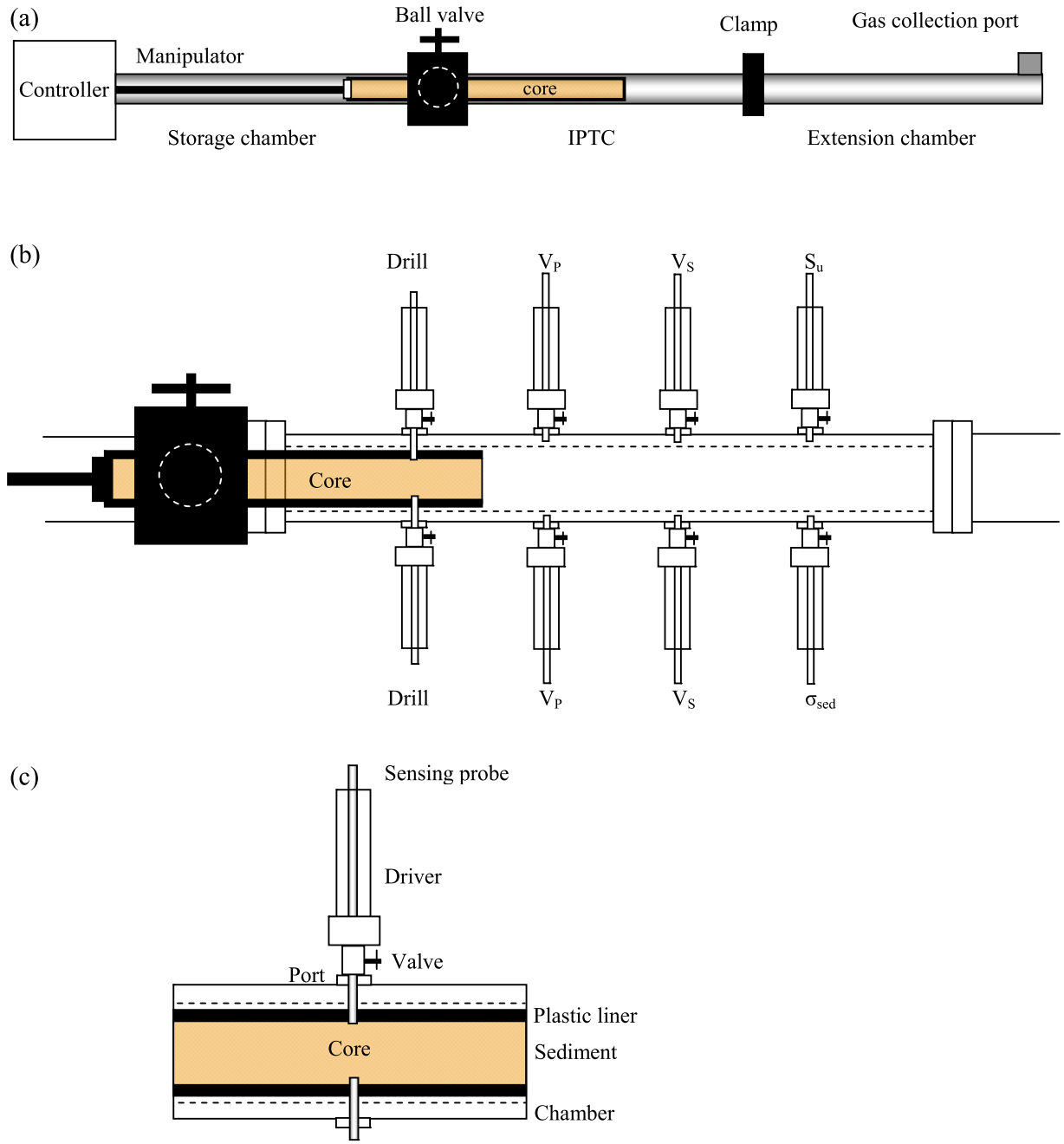

Figure 1. Configuration of the instrumented pressure testing chamber (IPTC). The main chamber accommodates eight ports, configured here with 6 probes and 2 drills. The IPTC is connected to the extension chamber on one end, and to the storage chamber and manipulator at the other end. (a) Complete device configuration. (b) IPTC chamber. (c) Close-up of the pressure core inside the IPTC. V_P, P wave velocity measurement; V_S, S wave velocity measurement; σ_{sed}, electrical conductivity of sediment measurement; S_u, undrained shear strength. A thermocouple replaces a strength probe during the depressurization test.

normally consolidated clay [*Santamarina et al.*, 2001]. The computed reference value of V_S = 338 m/s is shown as a dashed line in Figure 3c. The measured V_S values (solid circles) are lower than this reference value, implying the sediments have lost in situ effective stress and the local presence of hydrates does not contribute to skeletal shear stiffness. On the other hand, the shear wave velocity measured parallel to the hydrate veins at 30 and 40 cm locations shows $V_S \approx 1000$ m/s (solid triangle); for reference, a reported value for massive methane hydrate is $V_S \approx 1950$ m/s [*Helgerud et al.*, 2009].

3.2.4. Undrained Shear Strength

[16] The undrained shear strength S_u (Figure 3d) of uncemented normally consolidated clayey sediment at in situ conditions is controlled by σ'_v; a typical empirical correlation is $S_u = 0.22 \cdot \sigma'_v$ [*Mesri*, 1989]. Then, the estimated

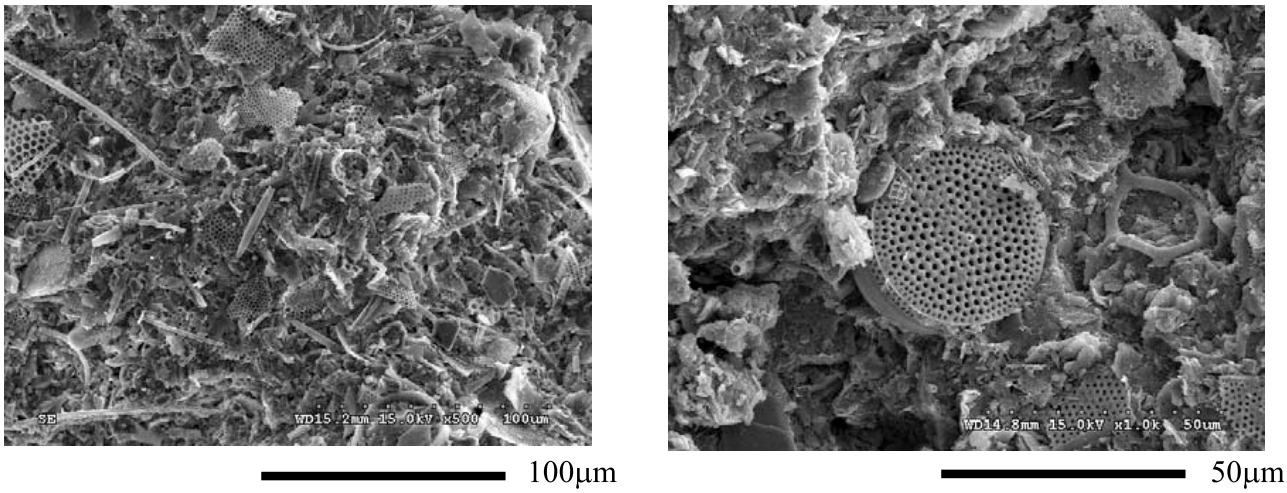

Figure 2. Scanning electron microscope images highlight the overwhelming presence of diatoms (sample from the 10B-17P core).

reference value for this core is $S_u \approx 286$ kPa (dashed line in Figure 3d). The measured undrained shear strength away from hydrate veins varies from 60 to 210 kPa (solid circles). The discrepancy between measured and reference values reflects two effects. First, the undrained shear strength S_u is expected to be less than the estimated in situ value because the sediments are tested at virtually zero effective stress inside the IPTC. The $S_u > 0$ results reflect the remaining sediment memory of past stress stored at lower sediment porosity. Second, this soft sediment has experienced extensive sampling effects (details discussed later in this manuscript) that result in a quasi disrupted and weakened sediment skeleton.

3.2.5. Electrical conductivity

[17] The electrical conductivity (Figure 3e) of sediments is determined by the pore fluid conductivity σ_{fl} and the sediment porosity n [*Archie*, 1942]. The reference sediment conductivity without hydrates is estimated to be $\sigma_s = 3.3 \pm 1$ S/m based on logging data (J.-J. Bahk, personal communication, 2010). For a nominal sediment conductivity of $\sigma_s =$ 3.3S/m, the plotted segments show the range of electrical conductivity values measured during each insertion of the electrical needle probe into sediments. Although the lower values detected at all tested location than the reference value hint the existence of hydrates, the integrated analysis with multiple properties is required to strengthen the presence and characteristic features of hydrates based on conductivity results.

3.3. Degassing of Gas Hydrates by Depressurization in the IPTC

[18] The evolution of pressure and temperature for the three pressure cores (10B-14R, 10B-17P and 10B-12P) during depressurization are plotted in Figure 4. The phase boundary for methane hydrate using CSMHYD software in pure water and NaCl 5 wt % solution is superimposed on Figure 4. Temperature remains constant until the pore pressure meets the phase boundary. The P-T conditions then follow the phase boundary during hydrate dissociation and deviate from the boundary afterward. Minor differences in P-T trajectories relative to the phase boundary likely result from nonequilibrium conditions caused by fast depressurization and noncolocated pressure and temperature sensors that are not in continuous contact with the hydrate dissociation front. Note that the thermocouple replaced the S_u probe.

[19] The sample cores were X-ray scanned before and after depressurization. Fluid pressure, sediment temperature, produced gas volume, S and P wave velocity are continuously monitored at fixed locations. X-ray images for the 10B-17P core sample in Figure 5a show that distinctive features such as hydrate veins vanish after depressurization and the sediment stratification becomes unclear due to gas liberation and fluid/gas migration out of the sediment. The evolution of measured properties is shown in Figures 5b–5f. The sediment temperature remains almost constant until the pressure reaches the phase boundary at $T_s = 3.5$°C (Figures 5b

Table 1. Index Properties of the Tested Sediments[a]

Property	Specimens				Methods
	10B-12P	10B-17P	9C-7R	10B-14R	
Specific gravity, G_s	2.61	2.57	2.59	2.64	ASTM D854
Specific surface, S_a (m^2/g)	27	31	21	31	N_2 adsorption
Clay content (%)	18	12	32	38	less than 2 μm
Liquid limit, w_L	78	115	90	67	ASTM D4318
Plastic limit, w_P	40	65	52	34	ASTM D4318
Plastic index, PI = $w_L - w_P$	38	50	38	33	
Soil classification	OH or MH	OH or MH	OH or MH	OH or MH	USCS system

[a]Test procedures and additional data are from *Lee et al.* [2011].

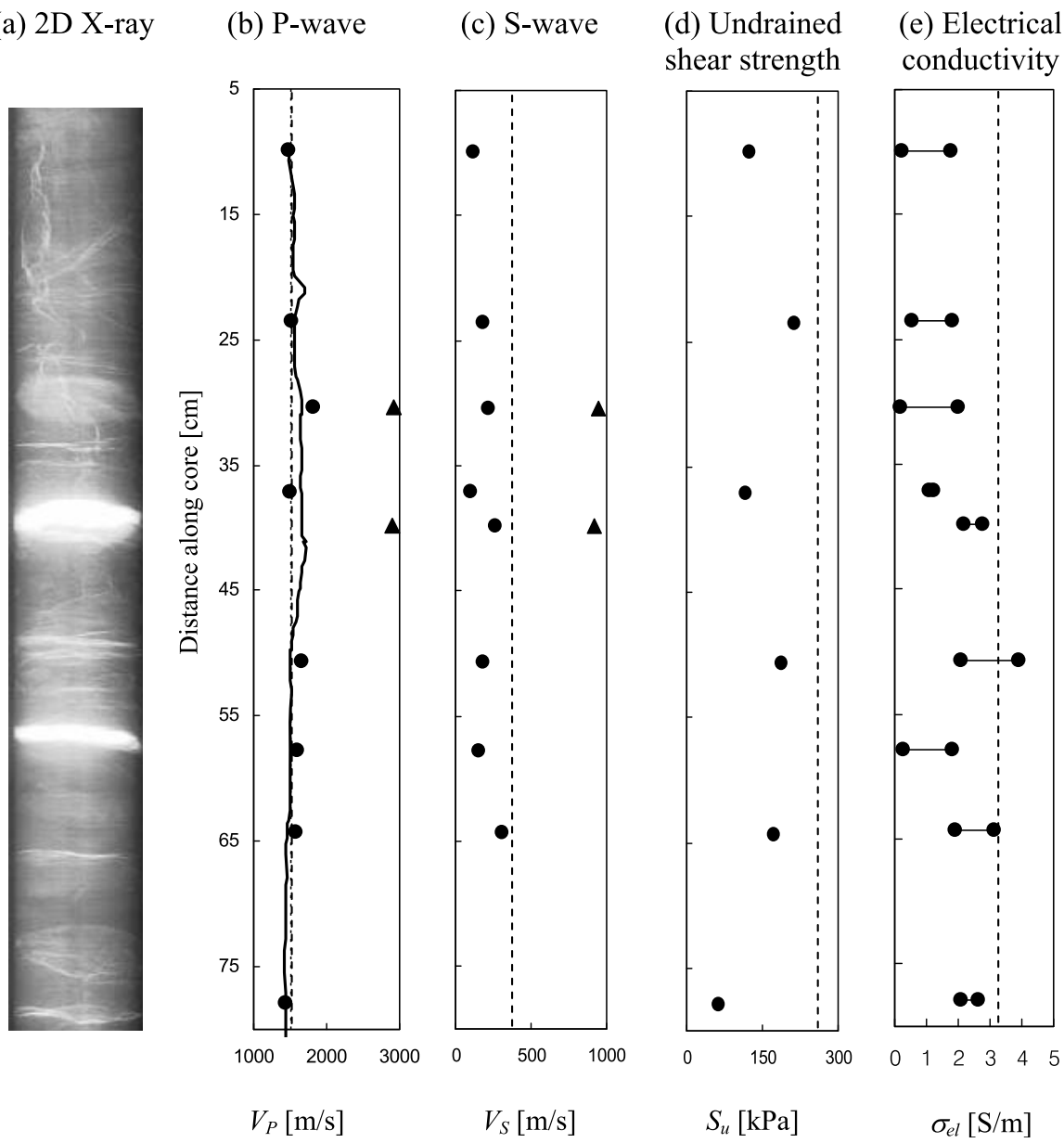

Figure 3. Data summary for one pressure core (10B-17P). X-ray images (from GeoTek) and properties measured inside the IPTC. Solid circle, data at general locations. Solid triangles, measured values parallel to horizontal hydrate veins. The plotted undrained shear strength S_u is the maximum value, while the electrical conductivity σ_{el} is the minimum value obtained in each penetration. Estimated reference values (refer to text): seawater $V_P \approx 1500$ m/s; sediment without hydrate $V_S = 338$ m/s; undrained shear strength $S_u = 0.22\sigma' = 286$ kPa; electrical conductivity of the sediment from logging data $\sigma_s = 3.3$ S/m. Note that solid line in Figure 3b shows data measured by noncontact low-frequency transducers (~500 kHz, GeoTek's MultiSensor Core Logger). Dashed lines refer to reference values for hydrate-free sediments.

and 5c); the temperature then gradually drops to $T_s \approx 1.2$°C, roughly following the phase boundary as a result of endothermic hydrate dissociation and gas depressurization. Gas starts coming out of the chamber after ~100 min when $P = 4.7$ MPa and $T_s = 3.0$°C (still along the phase boundary, Figure 5d).

[20] While hydrate is present, pressure recovers toward P-T conditions on the phase boundary. The duration of each depressurization steps is typically shorter than the time required for P-T stabilization. The mass of the entire chamber is kept constant for 8 h to achieve the equilibrium pressure and temperature ($t = 180$ min to $t = 650$ min); there is a slight rebound in pressure from 3.2 to 3.7 MPa while T_s is constant at 1.2°C (Figures 5b and 5c). Further depressurization causes the temperature to drop below 0°C and significantly below the phase boundary due to the decompression of the gas phase. The concurrent events (e.g., exothermic reaction by ice formation and endothermic reaction by hydrate dissociation) complicate the temperature signature. The onset of massive gas collection did not begin until $t = 115$ min

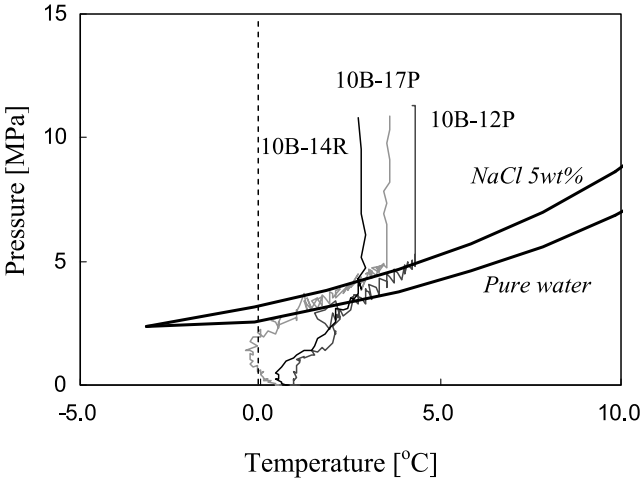

Figure 4. Evolution of pressure and temperature during gas production by controlled depressurization of three pressure cores inside the IPTC. The stability curve for methane hydrate is constructed for the case of pure water and ionic concentration of 5 wt % using CSMHYD software (available at http://hydrates.mines.edu/CHR).

(Figure 5d), even though the sediment reached the phase boundary and hydrates started dissociating at $t = 45$ min. This time delay likely indicates gas entrapment within the sediment. Note that the gas collection port was located at the end of extension chamber (see Figure 1) that was ~1.5 m away from the core and the entire system was slightly uplifted toward the gas collection port to readily collect any entrapped gas in the system.. Successive dissociation of hydrates after reaching the phase boundary at $t = 45$ min would increase the gas pressure within the sediment, while leaving behind gas escape paths. The final volume of collected gas and water are V_g = 38.6 L and V_w = 2.2 L at atmospheric pressure. The hydrate number χ in $CH_4 \cdot \chi H_2O$ varies from 5.81 to 6.1 considering the cage occupancy and the corresponding conversion factor C between volume of gas and volume of hydrate becomes $C = V_g/V_h = 164.1–171.2$ at 1 atm and 4°C [*Circone et al.*, 2005; *Kwon et al.*, 2008]. As the produced water volume is correlated with the initially existing hydrate volume as well, the hydrate volume becomes $V_h = (V_g + V_w - V_{gd})/C$, where V_{gd} is the volume of decompressed gas that is dissolved in pore fluid. The computation of V_{gd} involves the iterative process starting with the initial guess of pore fluid volume. Using the nominal values of solubility ~0.061 mol/kg at 4°C, 13 MPa and 5 wt % of salinity under clathrate equilibrium condition and density ~4.4×10^{-5} mol/cm^3 at 4°C and 1 atm for methane gas [*Lide*, 1995; *Duan and Mao*, 2006] (note that both values are obtainable using online calculator available at http://www.geochem-model.org), the volume of hydrate V_h ranges from 230.7 to 240.7 cm^3. The pore space hydrate saturation in the sediment is estimated to be $S_h = V_h/V_v = V_h/(nV_{specimen}) = 19.1–19.9\%$ (average value of 19.5% for $\chi = 5.99$) for the 82.2 cm long, 5 cm diameter core, with in situ neutron porosity $n = 0.75$.

[21] The initial S wave velocity V_S = 170 m/s remains constant until P-T conditions reach the phase boundary (Figure 5e). The velocity then decreases to reach 35 m/s at atmospheric pressure. This trend captures the loss of sediment global stiffness due to the volume expansion of liberated gas and associated soil skeleton disturbance during hydrate dissociation. The central frequency of S wave signals decreases during degassing because the resonant frequency of the sediment-coupled transducers is affected by the sediment stiffness (Figure 5f). Figure 6 shows the gradual decrease of travel time and frequency evolution of S wave signals during hydrate dissociation and gas escape. Markers i to iv in Figure 6 correspond to reference lines designated in Figure 5b to Figure 5c.

[22] The amplitude of P waves gathered during the degassing of the 10B-12P core vanishes as soon as P-T conditions reach the phase boundary and before gas is recovered outside the chamber (Figure 7). We did anticipate a pronounced decrease in P wave velocity as soon as a gas phase forms due to the high sensitivity of the pore fluid stiffness to the presence of soft gas bubbles, as predicted using Biot-Gassmann formulation (detailed discussion by *Santamarina et al.* [2001]). However, results in Figure 7 highlight that the rapid increase in attenuation as soon as gas bubbles form suppresses the signal, and hinders further analysis. These gas bubbles form at the onset of hydrate dissociation (dotted line i) though no gas reaches the gas collector until well after the P wave amplitude has vanished (dotted line ii).

4. Discussion

4.1. Hydrate Distribution in Sediments

[23] Hydrates appear to be segregated in 2-D X-ray projections. However, a detailed hydrate topology cannot be discerned from 2-D images. We therefore reconstructed 3-D tomographic images to visualize segregated hydrate lenses and veins in these sediments. Two nonconvolutional image processing steps were implemented.

[24] First, the original tomogram T was thresholded to expose all segregated hydrates. The histogram of pixel values in 2-D images (8 bit image type ranging from 0 to 255 pixel values; 0 for black and 255 for white) shows two characteristic peak values, and the peak centered at ~110 corresponds to "sediment pixels," while the second peak centered at ~190 represents "massive hydrate pixels." The thresholded image was obtained from a threshold value of ~125 and was expressed as a binary image B where 0 represents sediment (black) and 1 represents the hydrate mass (white). Speckles or noise pixels emerge due to the superposition of distribution tails, so there is some probability that thresholding designated some pixels as "material α" when they are actually "material β," and vice versa. Then, a "selective smoothing" step was implemented to despeckle all slices in B without smoothing: a pixel i, j in a despeckled slice of the final tomogram S was assigned with a value 0 or 1 depending on all values within a window size $N \times N$ centered at the location i, j in the corresponding slice of the original binary image B.

$$S_{i,j} = 1 \quad \text{if} \quad \left[\sum_{u=-(n-1)/2}^{(n-1)/2} \sum_{v=-(n-1)/2}^{(n-1)/2} B_{i+u,j+v} \right] \geq N^* \qquad \text{otherwise} \quad S_{i,j} = 0 \tag{1}$$

where N^* is the selective smoothing parameter. This selective smoothing step agrees with the inherent tendency to form segregated hydrate in fine grained sediments.

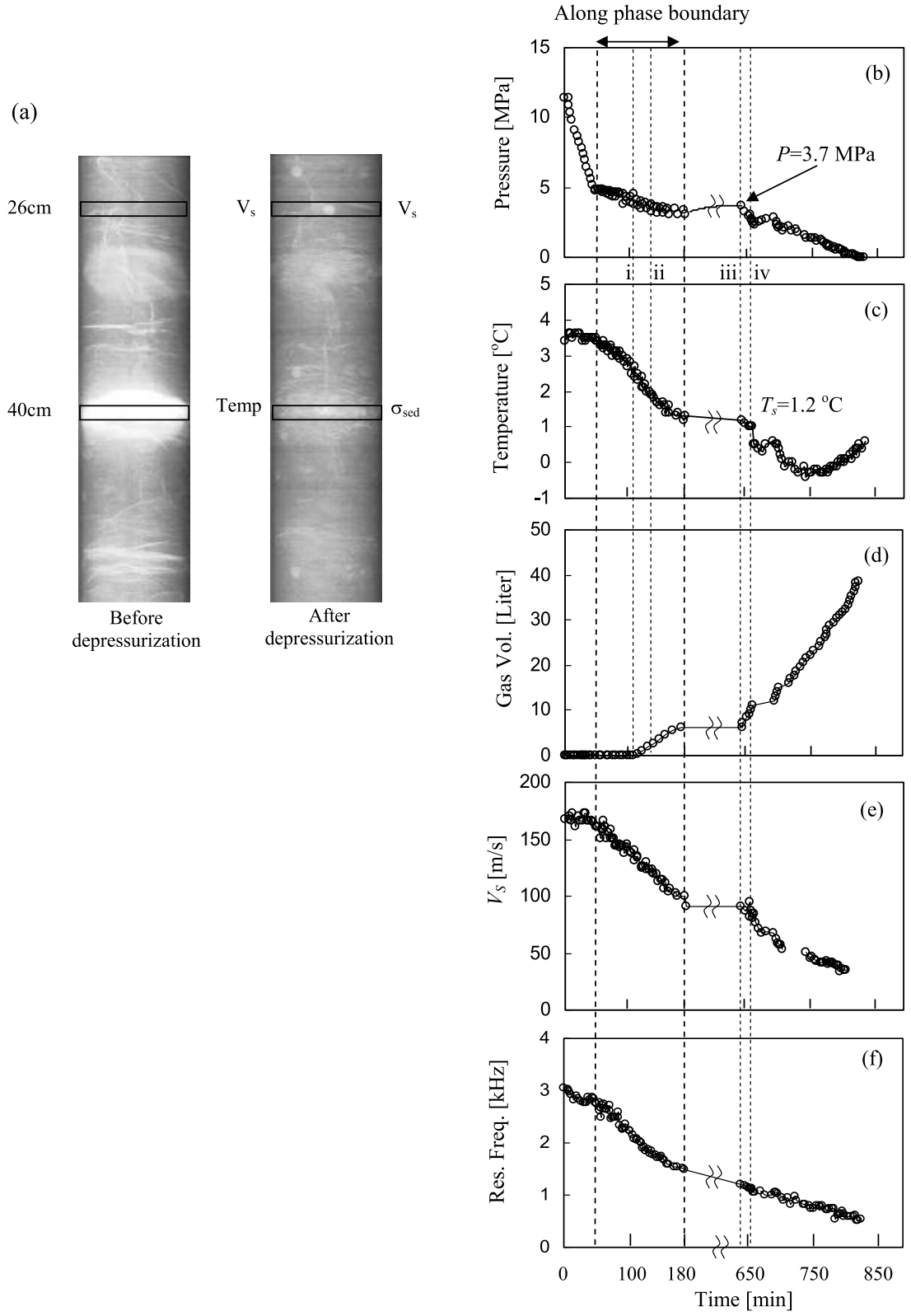

Figure 5. Evolution of physical properties and produced gas (volume at 1 atm) collected during depressurization of the 10B-17P pressure core: (a) X-ray images before and after dissociation (courtesy of GeoTek), (b) pressure, (c) temperature, (d) gas volume, (e) S wave velocity, (f) resonant frequency of the shear wave. Markers i, ii, iii, and iv correspond to pressure condition in Figure 6.

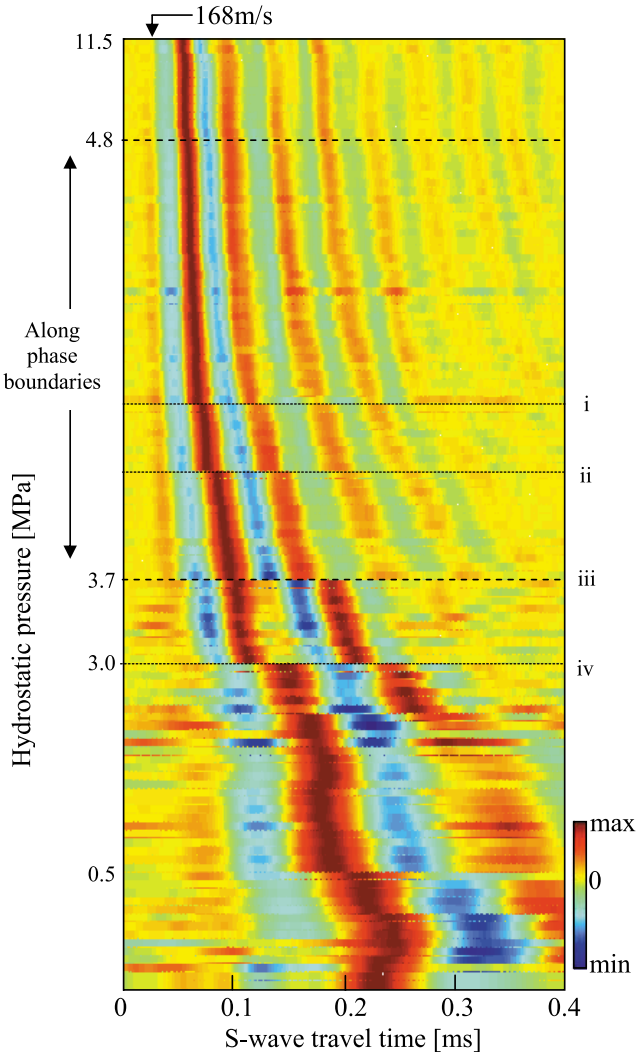

Figure 6. Evolution of S wavefield during depressurization of the 10B-17P pressure core (the corresponding wave velocity evolution is shown in Figure 5e). The amplitude is normalized by the maximum value of each signal. Markers i, ii, iii, and iv correspond to P-T conditions in Figures 5b–5f.

[25] Figure 8a shows the 2-D X-ray image (Figure 8a, left) and processed 3-D tomogram (Figures 8a, middle and right) for the 10B-17P core. The image in Figure 8a (middle) is obtained using at 10 × 10 smoothing window. The value of N^* used for selective smoothing in equation (1) is 55 to recover the experimentally measured mean hydrate saturation value S_h = 19.5% when χ = 5.99. The second filtered image shown in Figure 8a (right) was obtained using a larger window size 15 × 15 and a value N^* = 200. The resulting hydrate volume corresponds to a mean saturation of S_h = 11.4%. The dimension of filtered hydrate size corresponds to the value of $d_p^2 \times N^*$, where d_p is the pixel size (= 0.11 mm). It indicates that hydrates smaller than 0.67 and 2.42 mm^2 are removed by filtering with N^* of 55 and 200, respectively. These two results emphasize the dominant presence of segregated hydrate forming thick lenses and veins. The vertical vein in the upper 40 cm crosses horizontal hydrate layers whose thickness varies from millimeter to centimeter scales. Note that white strong and horizontal features in 2-D X-ray image are not fully correlated with the presence of hydrate lenses captured in 3-D image analysis. Thus, 2-D X-ray images do not necessarily capture most characteristic features of hydrates in pressure cores and require careful image analysis to conclude spatial distribution of hydrates.

[26] Figure 8b shows a 2-D X-ray image and a filtered 3-D tomogram for the 10B-18P core using a 10 × 10 window and N^* = 55. Vertical gas hydrate lenses bisect the core and cut through the regularly spaced horizontal hydrate veins. The computed hydrate volume corresponds to a hydrate saturation S_h = 22.2% of the pore space; as this core was not depressurized, there is no experimentally measured hydrate saturation for comparison.

4.2. Gas Production From Hydrate-Bearing Sediments

[27] Gas migration triggered by hydrate dissociation is limited by the sediment conductivity. The development of a percolating gas phase creates a mixed fluid condition, i.e., in order to mobilize through wet sediments, the gas must overcome the capillary pressure P_{cap}, which is a function of surface tension γ and pore size d_{pore} according to Laplace's equation

$$P_{cap} = \frac{4\gamma}{d_{pore}} \tag{2}$$

The mean pore size d_{pore} can be estimated from the sediment specific surface S_a and porosity n, $d_{pore} = \alpha n/[(1-n)S_a\rho_{min}]$, where ρ_{min} is the mass density of the mineral forming grains and α is the fabric coefficient $\alpha = 4 \pm 2$ [*Santamarina et al.*, 2001]. Gas-driven fractures will form if P_{cap} is significantly greater than the in situ effective stress σ'_o. For instance, the capillary pressure ranges from 1.68 MPa (α = 6) to 5.04 MPa (α = 2) and the in situ effective vertical stress is ~1.3 MPa at the depth of ~136 mbsf (assumed values are S_a = 40 m^2/g, ρ_{min} = 2500 kg/m^3, γ = 75.65 dyn/cm). Note that these values provide a first approximation and require further investigation for the in situ condition. Similarly, the dissociation of network-forming hydrate lenses observed in these sediments may leave behind preferential paths for gas migration. Therefore, the gas pressure caused by hydrate dissociation should be larger than the capillary pressure to create the gas escape path in these fine grained sediments and the path would not close in the absence of effective stress in the depressurized cores reported above. The interplay among the increased gas pressure by dissociation and subsequent decay due to gas migration, in situ effective stress and capillary pressure determines the fate of the sediment structure.

4.3. Potential Sampling Effects

[28] The effective stress release as the core travels through the cutting shoe can occur faster than the rate of pore pressure homogenization within the core. While the sediment tends to expand due to the removal of effective stress, the expansion of the sediment skeleton is temporarily hampered by fluid drainage in this undrained condition and the fluid pressure inside the core may fall below the phase boundary even if the external fluid pressure remains within the stability field. The hydrate dissociation would then cause the discontinuity (e.g., gas-driven fracture) in soils, followed by hydrate reformation into thin lenses when conditions

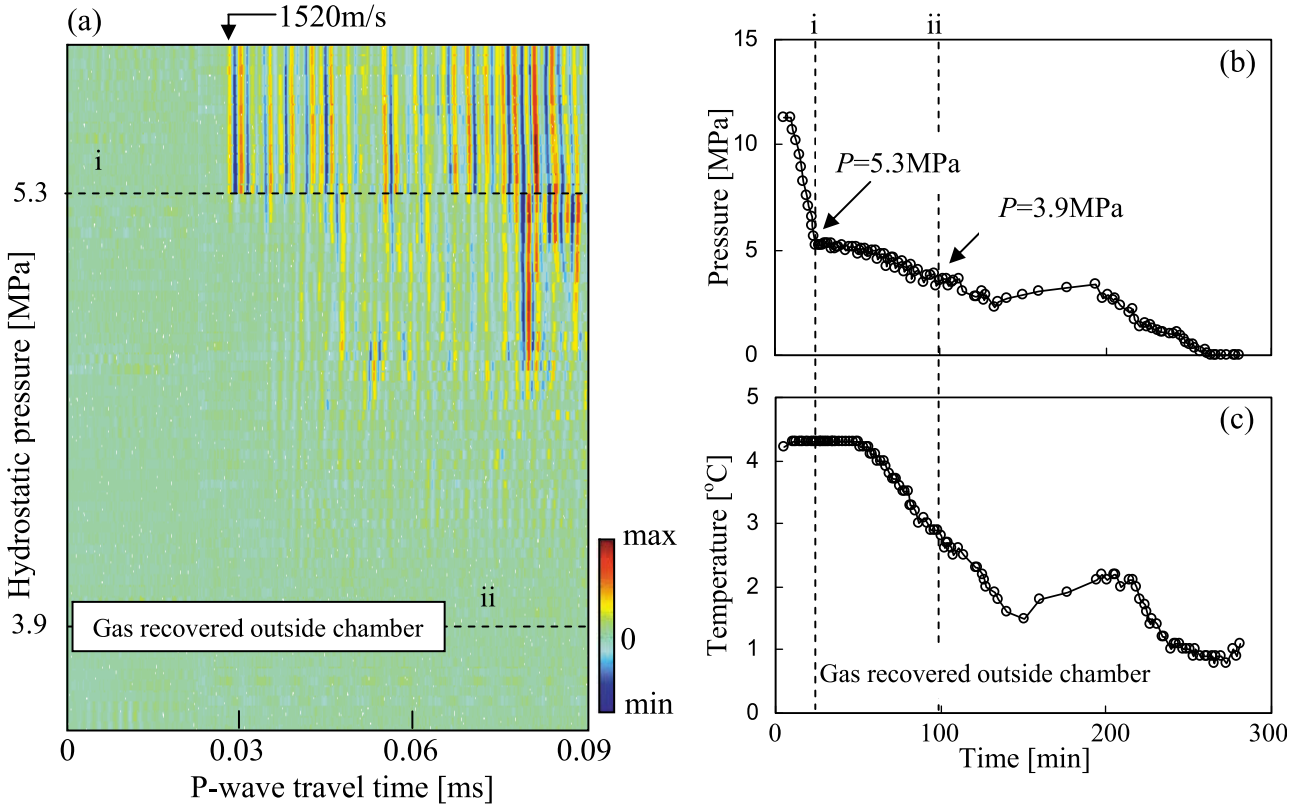

Figure 7. P-T conditions during the controlled depressurization of core 10B-12P, and the corresponding evolution of P wavefield. The signal amplitude is normalized by the maximum value of each signal. Lines i and ii show P-T conditions along the phase boundary. Note that gas recovery started even after the P-T condition reaches to the phase boundary.

return to the stability field of hydrates. Scale analysis indicates that coring velocity v should be lower than $v = 4c_v/d$, where d is the core diameter, to avoid this undrained poroelastic effect. The coefficient of consolidation for most clayey sediments is $c_v < 10^{-3}$ cm/s. Undrained coring is anticipated in most coring operations, and fine-grained sediment may develop hydrate-filled lens-type features as a result.

[29] Additional coring effects result from the rotational coring tool [*Arman and McManis*, 1977; *Young et al.*, 1983]. Figure 9 shows evidence of striation from the cutting shoe in 2-D X-rays and 3-D tomograms of 10B-5R and 10B-14R core samples recovered using the rotary cutting method (i.e., Hyace Rotary Core).

[30] We have observed the longitudinal rotation of diametrical hydrate lenses in some cores; this feature may result from the combined effects of sudden depressurization and torsional shear effects discussed above. These observations suggest the need for careful analysis of hydrate distribution and lens orientation.

4.4. Stiffness Change During Degassing

[31] The formation of a gas phase during depressurization produces marked changes in both P and S wave propagation, as shown in Figures 5, 6, and 7. Velocities V_P and V_S are related to bulk density, bulk and shear stiffness K and G according to $V_P = \sqrt{(K_{\mathrm{hbs}} + 4G_{\mathrm{sk}}/3)/\rho}$ and $V_S = \sqrt{G_{\mathrm{sk}}/\rho}$ where subindices indicate hbs for hydrate-bearing sediment and sk for sediment skeleton. The following discussion explores the effects of hydrate dissociation on K_{hbs} and G_{sk}.

[32] Changes in bulk stiffness are readily explained because the low bulk stiffness of gas K_g lowers the global bulk stiffness of the hydrate-bearing sediment K_{hbs} relative to the gas-free state [*Santamarina et al.*, 2001]:

$$K_{\mathrm{hbs}} = K_{\mathrm{sk}} + \left[\frac{1-n}{K_m} + n\left(\frac{S_h}{K_h} + \frac{S_w}{K_w} + \frac{S_g}{K_g}\right)\right]^{-1} \quad (3)$$

where n stands for porosity and subindices denote w for water, h for hydrate, m for mineral that makes the sediment grains, and g for gas. The analysis of common conditions in hydrate-bearing sediments shows that gas saturation as low as $S_g = 0.1\%$ causes a detectable decrease in P wave velocity.

[33] The presence of hydrates increases the sediment shear stiffness G_{sk}. Hydrate distribution determines the sensitivity of G_{sk} to S_h (see review by *Waite et al.* [2009]). Cementing hydrate formed at contacts has the highest effect on G_{sk} (e.g., water-limited hydrate formation in sands so that water at interparticle contacts forms hydrate). In the case of hydrate formation in gas-limited water saturated sands, hydrate forms away from interparticle contacts and has a lesser effect on stiffness, particularly when the hydrate saturation is lower than 40%. There is no controlled laboratory data on the effect of segregated hydrate on the shear stiffness of hydrate-bearing clays, though both upper and lower Hashin-Shtrikman bounds anticipate an increase in global stiffness.

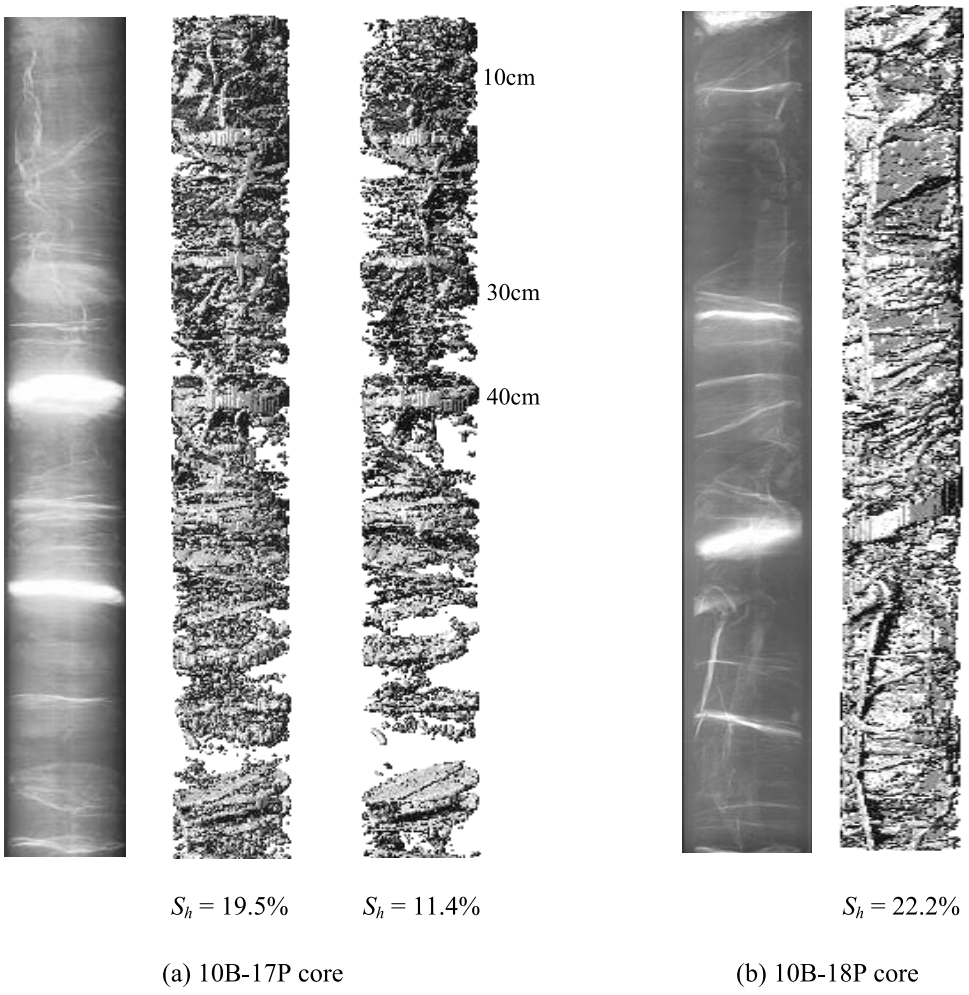

Figure 8. Hydrate distribution. (a) 10B-17P core: (left) 2-D X-ray plate; (middle) filtered 3-D tomogram with a threshold N^* = 55 and a window of 10 × 10 pixels; (right) filtered with N^* = 200 and 15 × 15 pixel window. (b) 10B-18P core: (left) 2-D X-ray plate; (right) filtered 3-D with a threshold N^* = 55 and a window of 10 × 10 pixels (X-ray and original tomographic data courtesy of GeoTek).

Conversely, we conclude there will be a decrease in shear stiffness G_{sk} during hydrate dissociation in any kind of sediment. The lower shear wave velocity V_S and frequency in Figure 5 and the longer travel times in Figure 6 are in agreement with this conclusion.

[34] Finally, we observe a very marked increase in P wave attenuation as soon as the sediment touches the phase boundary and gas begins to form (Figure 7). This reflects the emergence of high-loss, pore-scale mechanisms such as local fluid flow and cyclic liberation of the gaseous phase due to the discrete depressurization and subsequent degassing [*Palmer and Traviolia*, 1980; *Winkler and Nur*, 1979]. The P wave in particular are affected because attenuation increases with frequency and P wave measurements are conducted at higher frequencies ($f \approx 1$ MHz) than the S wave measurements ($f \approx$ 1–2 kHz).

4.5. Diatomaceous Marine Sediment

[35] There are several well-established empirical correlations to estimate engineering design parameters for fine grained sediments in terms of index properties such as plasticity. However, these correlations should be applied with caution when diatomaceous marine sediments are involved. The internal porosity of diatoms implies a higher surface area than for solid grains of the same size. Furthermore, internal pores retain water and a higher apparent plasticity is inferred, which biases the sediment classification. Compared to other sediments of the same plasticity, diatomaceous soils have higher strength and friction angle (due to interlocking between diatoms), higher hydraulic conductivity (due to interskeletal and intraskeletal structure), and higher compressibility at high stress (due to breakage of diatom skeletons) [*Shigomatsu et al.*, 2006; *Tanaka and Locat*, 1999].

[36] The development of gas production strategies from hydrate-bearing sediments in the Ulleung Basin must recognize the unique geomechanical characteristics of diatomaceous soils; their relatively low fluid conductivity; hydrate distribution in the form of segregated lenses and veins; the possibility of gas pressure buildup during heat-driven production and the formation of gas-driven fractures; volume

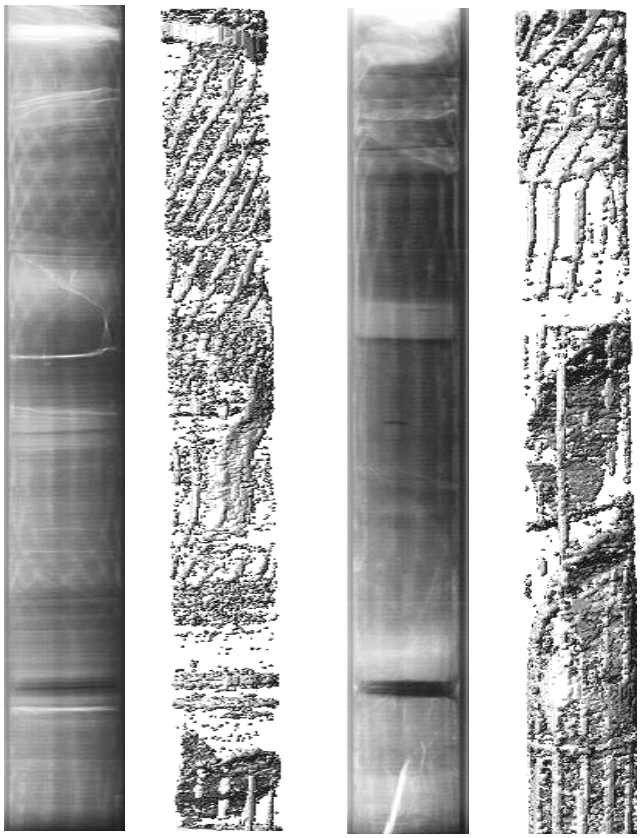

(a) 10B-5R core (b)10B-14R core

Figure 9. Sampling effects. Rotary coring (Hyace Rotary Core): (a) 10B-5R core and (b) 10B-14R core. The striated pattern left by the cutting shoe of the rotary corer captures the relative rotation between the sediment and the cutting shoe during coring. A diagonal pattern corresponds to simultaneous tool rotation and longitudinal displacement. A vertical pattern indicates the longitudinal displacement of the tool without relative sediment-shoe rotation. Sudden discontinuities indicate the torsional shear of the sediment. Torsional shear also manifests itself in the rotation of diametrical thin lenses found along the core when sequentially viewing slices along 3-D tomograms of cores.

contraction associated to segregated hydrate dissociation and possible diatom crushing (the latter in depressurization-driven production); and associated stability implications.

5. Conclusions

[37] Seven pressure cores were recovered during the UBGH Expedition 01 and maintained within hydrate P-T stability conditions throughout the recovery, imaging, and physical property measurement steps. Afterward, three cores were subjected to controlled and monitored depressurization. Finally, depressurized sediments were analyzed to characterize the sediment.

[38] Microfossils make up the bulk of the Ulleung Basin sediment mass. This particular constitution and fine-grained fabric determine hydrate distribution, physical properties, and the potential selection of gas production strategies.

[39] The physical properties of hydrate-bearing sediments are affected by the spatial distribution of hydrates. Pressure cores recovered at the Ulleung Basin show hydrate very heterogeneously distributed as veins, lenses and nodules. Though pressure coring technology was used to preserve the in situ hydrate distribution, some of segregated features may be the result of poroelastic effects during coring and sampling.

[40] Pressure cores were tested within the stability field, but under virtually no effective stress. Even so, the sediment retains a portion of the effective stress the sediment experienced in situ. These observations and estimated reference values for sediments at in situ conditions but without hydrates facilitated data interpretation. In particular, regions of high hydrate saturation and solid hydrate veins exhibited high P and S wave velocities.

[41] Three cores were subjected to controlled depressurization tests while pressure, temperature, P or S wave propagation, electrical conductivity, and the amount of produced gas were continuously monitored. The P wave propagation data clearly captures the initiation of hydrate dissociation. The lower attenuation of S waves under mixed fluid conditions permits tracking the evolution of shear stiffness throughout the complete dissociation process.

[42] Chemical and thermal driven dissociations may trigger gas pressure build up in these diatomaceous sediments. Gas driven fractures and preferential high-conductivity paths along segregated hydrate planes may form and remain open as long as the gas pressure exceeds the in situ effective stress conditions. These high-conductivity planes may facilitate gas migration and recovery.

[43] **Acknowledgments.** Support for this research was provided by a contract to T. S. Yun from the Korea Institute of Geoscience and Mineral Resources (KIGAM), Gas Hydrate Development Organization, and the Ministry of Knowledge Economy in Korea. Support for the development of the IPTC chamber was provided by the JIP-DOE grant to J. C. Santamarina. Peter Schultheiss, Melanie Holland, and Matt Druce from GeoTek, Inc. and collaborators at KIGAM provided technical support during the laboratory testing in Korea. All findings by authors do not reflect the views of funding agencies or technical support personnel.

References

Archie, G. E. (1942), The electrical resistance log as an aid in determining some reservoir characteristics, *Trans. Am. Inst. Min. Metall. Pet. Eng.*, *146*, 54–62.

Arman, A., and K. L. McManis (1977), Effects of conventional soil sampling methods on the engineering properties of cohesive soils in Louisiana, *Eng. Res. Bull. 117*, 310 pp., Div. of Eng. Res., La. State Univ., Baton Rouge.

Bahk, J. J., S. K. Chough, and S. J. Han (2000), Origins and paleoceanographic significance of laminated muds from the Ulleung Basin, East Sea (Sea of Japan), *Mar. Geol.*, *162*(2–4), 459–477, doi:10.1016/S0025-3227(99)00079-1.

Circone, S., S. H. Kirby, and L. A. Stern (2005), Direct measurement of methane hydrate composition along the hydrate equilibrium boundary, *J. Phys. Chem. B*, *109*, 9468–9475, doi:10.1021/jp0504874.

Duan, Z., and S. Mao (2006), A thermodynamic model of calculating methane solubility, density and gas phase composition of methane-bearing aqueous fluids from 273 and 523 K and from 1 to 2000 bar, *Geochim. Cosmochim. Acta*, *70*, 3369–3386, doi:10.1016/j.gca.2006.03.018.

Haacke, R. R., R. D. Hyndman, K.-P. Par, D.-G. Yoo, I. Stoian, and U. Schmidt (2009), Migration and venting of deep gases into the ocean through hydrate-choked chimneys offshore Korea, *Geology*, *37*(6), 531–534, doi:10.1130/G25681A.1.

Helgerud, M. B., W. F. Waite, S. H. Kirby, and A. Nur (2009), Elastic wave speeds and moduli in polycrystalline ice Ih, sI methane hydrate, and sII methane-ethane hydrate, *J. Geophys. Res.*, *114*, B02212, doi:10.1029/2008JB006132.

Hillier, S., B. K. Son, and B. Velde (1996), Effects of hydrothermal activity on clay mineral diagenesis in Miocene shales and sandstones from the Ulleung (Tsushima) back-arc basin, East Sea (Sea of Japan), Korea, *Clay Miner.*, *31*(1), 113–126, doi:10.1180/claymin.1996.031.1.10.

Hong, Z., Y. Tateishi, and J. Han (2006), Experimental study of macro- and microbehavior of natural diatomite, *J. Geotech. Geoenviron. Eng.*, *132* (5), 603–610, doi:10.1061/(ASCE)1090-0241(2006)132:5(603).

Huh, S., J. H. Chun, S. J. Han, H. S. Yoo, S. R. Kim, H. J. Kim, D. L. Choi, and Y. K. Lee (1999), Distribution, characteristics, and depositional environments of gas-charged sediment in the southeastern Ulleung Basin, the East Sea, *J. Geol. Soc. Korea*, *35*(3), 201–212.

Kargl, S., P. Y. Chenet, B. Yoo, and H. G. Im (2006), Petroleum system analysis for a Back-Arc Basin Offshore South Korea—The Ulleung Basin, paper presented at 68th European Association of Geoscientists and Engineers Conference and Exhibition, incorporating SPE EUROPEC 2006, EAGE 2006: Opportunities in Mature Areas, Vienna, Austria.

Kim, I. S., M. H. Park, Y. Lee, B. J. Ryu, and K. M. Yu (2003), Geological and Geochemical studies on the late Quaternary sedimentary environment of the southwestern Ulleung Basin, East Sea, *Econ. Environ. Geol.*, *36*(1), 9–15.

Kwon, T.-H., G.-C. Cho, and J. C. Santamarina (2008), Gas hydrate dissociation in sediments: Pressure-temperature evolution, *Geochem. Geophys. Geosyst.*, *9*, Q03019, doi:10.1029/2007GC001920.

Lee, C., T. S. Yun, J.-S. Lee, J. J. Bahk, and J. C. Santamarina (2011), Geotechnical characterization of marine sediments in the Ulleung Basin, East Sea, *Eng. Geol.*, *117*, 151–158, doi:10.1016/j.enggeo.2010.10.014.

Lee, H. J., S. S. Chun, S. H. Yoon, and S. R. Kim (1993), Slope stability and geotechnical properties of sediment of the southern margin of Ulleung Basin, East Sea (Sea of Japan), *Mar. Geol.*, *110*(1–2), 31, doi:10.1016/0025-3227(93)90103-3.

Lee, J. H., Y. S. Baek, B. J. Ryu, M. Riedel, and R. D. Hyndman (2005), A seismic survey to detect natural gas hydrate in the East Sea of Korea, *Mar. Geophys. Res.*, *26*, 51–59, doi:10.1007/s11001-005-6975-4.

Lee, T., J.-H. Hyun, J. S. Mok, and D. Kim (2008), Organic carbon accumulation and sulfate reduction rates in slope and basin sediments of the Ulleung Basin, East/Japan Sea, *Geo Mar. Lett.*, *28*(3), 153–159, doi:10.1007/s00367-007-0097-8.

Lide, D. R. (1995), *CRC Handbook of Chemistry and Physics: A Ready-Reference Book of Chemical and Physical Data*, CRC Press, Boca Raton, Fla.

Mesri, G. (1989), Re-evaluation of $S_u = 0.22\sigma'_v$ using laboratory shear tests, *Can. Geotech. J.*, *26*(1), 162–164, doi:10.1139/t89-017.

Palmer, I. D., and M. L. Traviolia (1980), Attenuation by squirt flow in under saturated gas sands, *Geophysics*, *45*, 1780–1792, doi:10.1190/1.1441065.

Park, M.-H., I.-S. Kim, and J.-B. Shin (2003), Characteristics of the late Quaternary tephra layers in the East/Japan Sea and their new occurrences in western Ulleung Basin sediments, *Mar. Geol.*, *202*(3–4), 135–142, doi:10.1016/S0025-3227(03)00287-1.

Pettigrew, T. L. (1992), Design and operation of a wireline pressure core sampler (PCS), report, 269 pp., Ocean Drill. Program, Tex. A&M Univ., College Station. doi:10.2973/odp.tn.17.1992.

Ryu, B. J., M. Riedel, J.-H. Kim, R. D. Hyndman, Y.-J. Lee, B.-H. Chung, and I. S. Kim (2009), Gas hydrates in the western deep-water Ulleung Basin, East Sea of Korea, *Mar. Pet. Geol.*, *26*(8), 1483–1498, doi:10.1016/j.marpetgeo.2009.02.004.

Santamarina, J. C., K. A. Klein, and M. A. Fam (2001), *Soils and Waves*, 488 pp., John Wiley, New York.

Shigomatsu, H., S. Higashi, M. Nozowa, and A. Yashima (2006), *Geotechnical Properties of Cohesive Soil Acidified by Pyrite Inclusion*, Thomas Telford Serv., London.

Stoian, I., K.-P. Par, D.-G. Yoo, R. R. Haacke, R. D. Hyndman, M. Riedel, and G. D. Spence (2008), Seismic reflection blank zones in the Ulleung Basin, offshore Korea, associated with high concentrations of gas hydrate, paper presented at 6th International Conference on Gas Hydrates (ICGH 2008), Vancouver, B. C., Canada, 6–10 July.

Stokoe, K. H., J. N.-K. Lee, and S. H.-H. Lee (1992), Characterization of soil in calibration chambers with seismic waves, in *Calibration Chamber Testing*, edited by A.-B. Huang, pp. 363–376, Elsevier, New York.

Tanaka, H., and J. Locat (1999), Microstructural investigation of Osaka Bay clay: The impact of microfossils on its mechanical behaviour, *Can. Geotech. J.*, *36*(3), 493–508, doi:10.1139/cgj-36-3-493.

Waite, W. F., et al. (2009), Physical properties of hydrate-bearing sediments, *Rev. Geophys.*, *47*, RG4003, doi:10.1029/2008RG000279.

Winkler, K., and A. Nur (1979), Pore fluids and seismic attenuation in rocks, *Geophys. Res. Lett.*, *6*, 1–4, doi:10.1029/GL006i001p00001.

Young, A. G., G. W. Quiros, and C. J. Ehlers (1983), Effects of offshore sampling and testing on undrained soil shear strength, *Proc. Annu. Offshore Technol. Conf.*, *15*, 193–201, doi:10.4043/4465-MS.

Yun, T. S., G. A. Narsilio, J. C. Santamarina, and C. Ruppel (2006), Instrumented pressure testing chamber for characterizing sediment cores recovered at in situ hydrostatic pressure, *Mar. Geol.*, *229*(3–4), 285–293, doi:10.1016/j.margeo.2006.03.012.

J. J. Bahk, Petroleum and Marine Resources Division, Korea Institute of Geoscience and Mineral Resources, Yuseong, PO Box 111, Daejeon, 305-350, South Korea. (jjbahk@kigam.re.kr)

C. Lee and J. C. Santamarina, School of Civil and Environmental Engineering, Georgia Tech, 790 Atlantic Dr., Atlanta, GA 30332-0355, USA. (changho@gatech.edu; jcs@gatech.edu)

J.-S. Lee, Department of Civil and Environmental Engineering, Korea University, 1, 5-Ka, Anam-dong, Sungbuk-Ku, Seoul, 136-701, South Korea. (jongsub@korea.ac.kr)

T. S. Yun, School of Civil and Environmental Engineering, Yonsei University, 262 Seongsan-ro, Seodaemun-gu, Seoul 120-749, South Korea. (taesup@yonsei.ac.kr)